Thermal scattering law of $(C_2H_4)_n$: Integrating experimental data with DFT calculations

Kemal Ramić [a,*], Carl Wendorff [a], Yongqiang Cheng [b], Alexander I. Kolesnikov [b], Doug L. Abernathy [b], Luke Daemen [b], Goran Arbanas [b], Luiz Leal [c], Yaron Danon [a], Li (Emily) Liu [a]

[a] Rensselaer Polytechnic Institute, 110 8th St, Troy, NY, USA
[b] Neutron Scattering Division, Oak Ridge National Laboratory, Oak Ridge, TN, USA
[c] Institut de Radioprotection et de Sûreté Nucléaire (IRSN), Paris, France

ARTICLE INFO

ABSTRACT

Improvements in determination of the thermal scattering law of moderator materials (measuring, calculating and validating) are important for accurate prediction of neutron thermalization in nuclear systems. In this work a methodology for producing thermal scattering libraries from the experimental data for polyethylene $(C_2H_4)_n$ is discussed. Double differential scattering cross section (DDSCS) experiments were performed at the Spallation Neutron Source of Oak Ridge National Laboratory (SNS ORNL). New scattering kernel evaluations, based on phonon spectrum for $(C_2H_4)_n$, are created using the NJOY2016 code. Two different methods were used: direct and indirect geometry neutron scattering at ARCS and SEQUOIA, and VISION instruments, respectively, where the phonon spectrum was derived from the dynamical structure factor $S(Q,\omega)$ obtained from the measured DDSCS. In order to compare and validate the newly created library, the experimental setup was simulated using MCNP6.1. Compared with the current ENDF/B-VII.1, the resulting RPI $(C_2H_4)_n$ libraries improved both double differential scattering and total scattering cross sections. A set of criticality benchmarks containing $(C_2H_4)_n$ from HEU-MET-THERM resulted in an overall improved calculation of K_{eff}, although the libraries should be tested against benchmarks more sensitive to $(C_2H_4)_n$. The DFT + oClimax method is used and is shown to be most comprehensive method for analysis of moderator materials. The importance of DFT + oClimax method lies in the fact that it can be validated against all data measured at VISION, ARCS and SEQUOIA, and experimental total scattering cross section measurements.

© 2018 Elsevier Ltd. All rights reserved.

1. Introduction

As the accuracy of simulations advances in many areas of nuclear science, code packages such as the Monte Carlo N-Particle code (MCNP), Goorley et al. (2016), are highly dependent on the accuracy of current Evaluated Nuclear Data Files (for example ENDF/B-VII.1), Chadwick et al. (2996). These evaluated libraries contain different nuclear reaction data, and most relevant for this work, these libraries contain thermal neutron scattering cross sections. Evaluations are widely used in neutron transport codes, and in this work we used MCNP 6.1. Due to the lack of the experimental data in the thermal region, it is difficult to validate the simulations against actual measured quantities. For the most current evaluations the only available data for validation and benchmarking are total cross section measurements.

For most moderators, the current ENDF/B-VII.1 libraries were created using a theoretical phonon spectrum (or density of states). The ENDF/B-VII.1 library for polyethylene was created by Koppel, Houston and Sprevak in 1969 and was converted to ENDF 6 format in 1989 at Los Alamos National Lab. In 2016 new polyethylene library, using molecular dynamics to calculate the phonon spectrum, created by North Carolina State University Nuclear Reactor Program has been added to ENDF as ENDF/B-VIII.b5 library. These libraries were created to correctly reproduce the energy dependent total neutron scattering cross section, with less attention to double differential scattering cross sections (DDSCS). Little to no DDSCS experimental data exist, and they were rarely used in the evaluations. In Kirouac et al. (1966) performed DDSCS measurements on polyethylene but due to the high incident energies, 830 meV and above, the data was not sufficient to be used for the validation or creation of new thermal scattering libraries. The goal of this work was to obtain new experimental DDSCS data, use it to derive an experimental phonon spectrum, and establish a streamlined

---

* Corresponding author.
    E-mail address: kramic12@gmail.com (K. Ramić).

methodology for the creation of new thermal scattering libraries for different moderator materials. The importance of this work lies in the fact that it is an review of thermal neutron scattering for polyethylene from experimental and simulation aspects. This work includes a method of combining both experiments and simulations to guide the creation of new thermal library. Additionally, using the methodology developed here, thermal scattering libraries for other nuclear materials (e.g., lucite, alpha-quartz, and ice-1 h) have been created (Ramić et al., 2018). The need for this work becomes self explanatory when one looks at the results from the Section 3.1.1 for $(C_2H_4)_n$ DDSCS and total cross section comparison. Polyethylene in ENDF/B-VII.1 evaluation is one of the better and more consistent evaluations.

2. Thermal neutron scattering theory

There are two parts to neutron scattering: incoherent and coherent. If we imagine a neutron beam incident on a system of multiple constituent particles, the incoherent part would represent the sum of the effects created by waves that do not interfere with each other, while the coherent part is represented by the sum of effects of waves that do interfere with each other, MacFarlane and Kahler (2010). Both parts include elastic and inelastic scattering components. For elastic scattering, there is no change in the neutron energy, while in the inelastic scattering, incident neutron energy can be up-scattered (increase in neutron energy), or down-scattered (loss of energy). The incoherent approximation for the coherently scattering polycrystalline material, where the inelastic neutron scattering (INS) data from randomly oriented crystallites is averaged, is valid when the volume of the reciprocal space covered by the INS experiment is much larger than the volume of the Brillouin zone of the crystal.

The DDSCS represents the number of neutrons scattering into a solid angle, subtended by a detector onto the sample, $d\Omega$, at energy transfer, $d\hbar\omega$. For mono-atomic sample, as seen in Ramirez-Cuesta (2004), in incoherent approximation DDSCS can be represented as:

$$\frac{d^2\sigma}{d\Omega d\hbar\omega} = \frac{\sigma_b}{4\pi}\frac{\mathbf{k}'}{\mathbf{k}}S(Q,\omega), \tag{1}$$

where $\mathbf{k}'$ and $\mathbf{k}$ are wavevectors of final and initial neutron states respectively, $\hbar Q$ is the momentum transfer, σ_b represents bound scattering cross section, $S(Q,\omega)$ is the scattering law.

In NJOY2016, the code used for creating of ENDF thermal scattering libraries, DDSCS in incoherent approximation, is represented as MacFarlane and Kahler (2010):

$$\frac{d^2\sigma}{d\mu dE} = \frac{\sigma_b}{2k_BT}\sqrt{\frac{E'}{E}}S(\alpha,\beta), \tag{2}$$

where E and E' are the incident and scattered neutron energies respectively, μ is the cosine of the scattering angle, k_BT is the equilibrium temperature in eV (25 meV at 293.6 K), and $S(\alpha,\beta)$ is the scattering law. The relationship between $S(Q,\omega)$ and $S(\alpha,\beta)$ is given as:

$$S(Q,\omega) = \frac{\hbar S[\alpha(Q),\beta(\omega)]}{k_BT}, \quad \alpha = \frac{\hbar^2 Q^2}{2Am_nk_BT}, \quad \beta = \frac{\hbar\omega}{k_BT}, \tag{3}$$

where m_n is the mass of neutron, A is the ratio of the mass of the scattering atom to the neutron mass. The relationship between wavevector $\mathbf{k}$ and energy of neutron is:

$$E = \frac{\hbar^2 k^2}{2m_n}, \tag{4}$$

α and β are related respectively to the momentum transfer and energy transfer:

$$\alpha = \frac{E' + E - 2\mu\sqrt{E'E}}{Ak_BT}, \beta = \frac{E' - E}{k_BT}. \tag{5}$$

In the incoherent and Gaussian approximation, MacFarlane and Kahler (2010), the $S(\alpha,\beta)$ is:

$$S(\alpha,\beta) = \frac{1}{2\pi}\int_{-\infty}^{\infty}e^{i\beta\hat{t}}e^{-\gamma(\hat{t})}d\hat{t}, \tag{6}$$

where:

$$e^{\gamma(\hat{t})} = \alpha\int_{-\infty}^{\infty}P(\beta)[1 - e^{i\beta\hat{t}}]e^{-\beta/2}d\beta, \tag{7}$$

with:

$$P(\beta) = \frac{\rho(\beta)}{2\beta\sinh(\beta/2)}, \tag{8}$$

where $\rho(\beta)$ is the density of vibrational states (GDOS), and $\hat{t}$ is the time measured in units of $\hbar/k_BT$ seconds. Generalized density of states (GDOS) is DOS weighted by squared atomic eigenvectors of vibrational modes.

Since $(C_2H_4)_n$ is a hydrogenous material, the incoherent elastic component can be represented as:

$$\left(\frac{d^2\sigma}{d\mu dE}\right)_{incoh,el} = \frac{\sigma_b}{2}e^{-2WE(1-\mu)}, \tag{9}$$

where W is the Debye-Waller coefficient, and is equal to:

$$W = \frac{\lambda}{Ak_BT}, \tag{10}$$

where λ depends on GDOS:

$$\lambda = \int_{-\infty}^{\infty}P(\beta)e^{-\beta/2}d\beta. \tag{11}$$

The connection between $P(\beta)$ and $\rho(\beta)$ can be observed in Eq. 8. The total scattering cross section for $(C_2H_4)_n$ is equal to the sum of incoherent elastic and inelastic parts.

If we expand the time-dependent part of the exponential $e^{-\gamma(t)}$ from Eq. 6 we obtain:

$$e^{\gamma(\hat{t})} = e^{-\alpha\lambda}\sum_{n=0}^{\infty}\frac{1}{n!}\left[\alpha\int_{-\infty}^{\infty}P(\beta)e^{i\beta\hat{t}}e^{-\beta/2}d\beta\right]^n, \tag{12}$$

thus, we can rewrite Eq. 6 in terms of phonon expansion:

$$S(\alpha,\beta) = e^{-\alpha\lambda}\sum_{n=0}^{\infty}\frac{1}{n!}\alpha^n\frac{1}{2\pi}\times\int_{-\infty}^{\infty}e^{i\beta\hat{t}}\left[\int_{-\infty}^{\infty}P(\beta')e^{i\beta'\hat{t}}e^{-\beta'/2}d\beta'\right]^n d\hat{t}, \tag{13}$$

At n = 0 there is no exchange of energy between neutron and the scattering molecule, hence the scattering is elastic. According to Ramirez-Cuesta (2004), n = 0 quantum event (mode) correspond to Rayleigh line in Raman scattering, and it corresponds to elastic line in the inelastic neutron scattering.

3. Measurements and analysis

The experimental data have been measured at the Spallation Neutron Source (SNS) at Oak Ridge National Laboratory (ORNL). Although the focus of this report is solely on $(C_2H_4)_n$, three different instruments have been used to measure different moderator materials and subsequent reports on remaining moderator materials will be released. The instruments used for data collection are Fine-Resolution Fermi Chopper Spectrometer (SEQUOIA) Granroth et al. (0120), a wide Angular-Range Chopper Spectrometer (ARCS) Abernathy et al. (2012), and VISION Seeger et al. (2009). ARCS and SEQUOIA are similar in geometry and produce

comparable experimental quantities, so the measurements and analysis will be divided into two methods: ARCS/SEQUOIA method and VISION method.
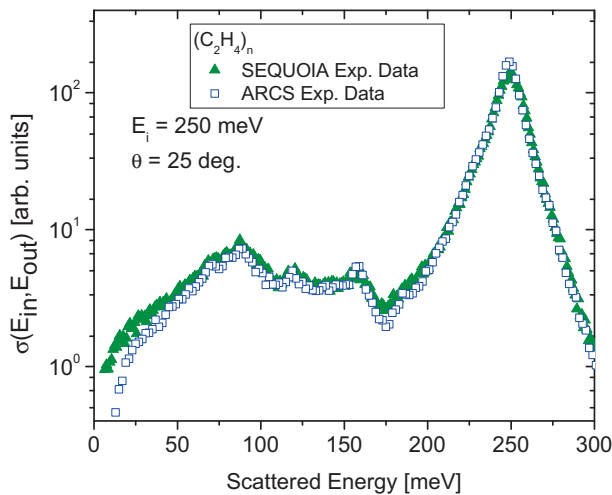
3.1. ARCS/SEQUOIA method

The DDSCS data for $(C_2H_4)_n$ were measured at SEQUOIA and ARCS, which are both time-of-flight direct geometry spectrometers. The incident neutron energies were selected by rotating Fermi choppers. The collected INS data were transformed from the time-of-flight and instrument coordinates to the dynamic structure factor S(Q,ω), corrected for the detector's efficiency. Background spectra from an empty container measured under similar conditions were subtracted from the sample data. The energy resolution of both spectrometers is in the range from 1 to 5% $\Delta E/E$.

Table 1 shows the summary of different (multiple incident energies and temperatures) measurements taken at both ARCS and SEQUOIA spectrometers. A comparison of $(C_2H_4)_n$ DDSCS between measurements taken at ARCS and SEQUOIA can be seen in Fig. 1. The measured data from both instruments correlates well. The slight nuances in the height of the peak in the lower energy region could be due to the difference in the structure of the sample material. The ARCS sample was semi-crystalline $(C_2H_4)_n$ in form of thin sheets, while the SEQUOIA sample was in the form of poly-crystalline $(C_2H_4)_n$ powder. Since the neutron scattering happens on a molecular level, more plausible explanation for the mismatch could be due to the different data processing procedures at the two different spectrometers.

For this report, the experimental data from ARCS was used. The sample material for $(C_2H_4)_n$, used for in-beam investigation, was HDPE (high density polyethylene) manufactured by Goodfellow corporation in 10 μm sheets. The neutron scattering of $(C_2H_4)_n$ is dominated by the large hydrogen incoherent scattering cross section. Thickness of the sample was chosen so that the neutron transmission is larger than 80%.
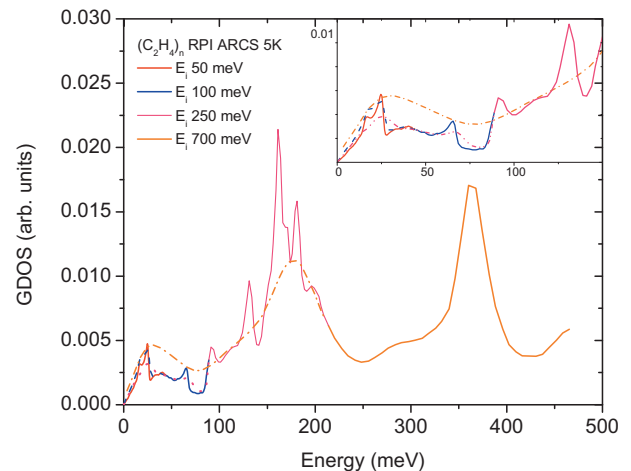
The analysis of the experimental data measured at ARCS was carried out using the DAVE suite, that is maintained by the National Institute of Standards and Technology (NIST) Azuah et al. (2009). In order to generate GDOS from DDSCS, the MSLICE module of the DAVE suite was used. As described in Squires (Squires, 2012), the dependence of GDOS to DDSCS ($S(Q,\omega)$) is:

$$S(Q,\omega) = \frac{\hbar^2 Q^2}{6M\omega} exp\left(-\langle u^2 \rangle Q^2\right) G(\omega) \left[n(\omega,T) + \frac{1}{2} \pm \frac{1}{2}\right], \tag{14}$$

$$n(\omega,T) = \frac{1}{exp(\frac{\hbar\omega}{kT}) - 1}, \tag{15}$$

where $G(\omega)$ is GDOS, ω is used as frequency (1/time), and it appears with $\hbar$ (as energy in units of meV), M is the atomic mass (for monoatomic material) of the scattering material, $n(\omega,T)$ is population Bose factor, $\langle u^2 \rangle$ is the atomic mean-square displacement (MSD), and $+$ or $-$ should be taken in the squared brackets for neutrons scattered with energy loss or energy gain, respectively.

The peculiar thing about the analysis of the experimental data is that for $(C_2H_4)_n$ at ARCS, the data were gathered for four incident energies: 50, 100, 250 and 700 meV. To envelop as much as possible of the (Q,ω) range with good energy and momentum transfer resolution, four different incident energies were used so that there was an overlapping energy region between the measurements. In order to produce the GDOS at uniform energy grid, the four data sets were collapsed into one. All four data sets have different normalization, and due to difficulty in finding a unique normalization constant, a different approach is needed. Lavelle et al. (2013) proposed a method for collapsing several data sets and provided a graphical representation of how the collapsing method is performed. In this method, a normalizing constant, between two adjacent incident energies, is calculated from the integrated area in a predetermined overlapping region. In order to reduce the multiphonon scattering, the relation $\langle u^2 \rangle Q^2 < 1$ had to be maintained; thus the data that did not comply with the criteria was rejected. $\langle u^2 \rangle$ for $(C_2H_4)_n$ was determined, using the method described in Lavelle et al. (2013), to be 0.0139 ± 0.001 Å^2 at 5 K; therefore Q has to be less than 8.5 Å^{-1}. The GDOS collapsing method is presented in Fig. 2, while the resulting GDOS can be seen in Fig. 3.

Table 1
Summary of experiments at SNS ORNL.

Moderator	SEQUOIA		ARCS	
	E_i [meV]	T [K]	E_i [meV]	T [K]
$(C_2H_4)_n$	55, 160, 250, 600, 1000, 3000, 5000	300	50, 100, 250, 700	5, 295

Fig. 1. ARCS versus SEQUOIA $(C_2H_4)_n$ DDSCS comparison at a scattering angle of 25 degrees and the 250 meV incident energy of the neutron. The ARCS sample was measured at 295 K while SEQUOIA sample was measured at 300 K.

Fig. 2. The process of normalizing GDOS using the set of four incident energies, 50, 100, 250, and 700 meV. The inset shows the solid lines, out of which final GDOS is created, and dashed lines, which represent the data from higher incident energies that were rejected.
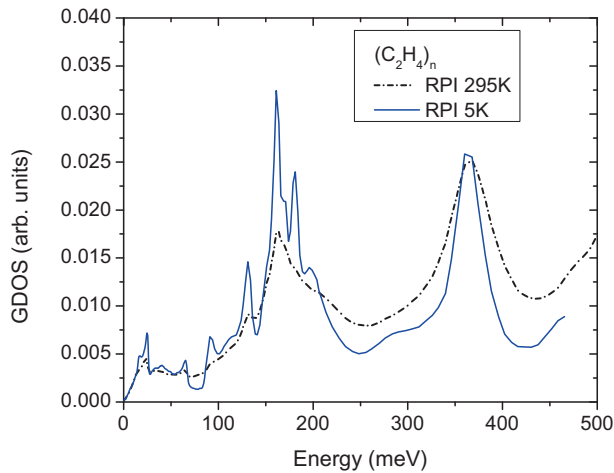
Fig. 3. The resulting $(C_2H_4)_n$ GDOS derived from measurements at 5 K and 295 K.

The GDOS at 5 K exhibits sharper structure, which is due to the fact that at 5 K multi-phonon effects are diminished, albeit not completely suppressed, and at higher temperatures the GDOS tends to smoothen out due to the over-amplification of effects quasi-elastic modes, rotational excitations, and Debye-Waller effect. For the following analysis, we used 5 K data for the creation of new scattering law for $(C_2H_4)_n$. The method used to collapse GDOS onto the same energy range does not necessarily preserve the ratio of areas under the peaks, resulting in inaccurate total scattering cross section when compared to a theoretical GDOS; therefore an adjustment was required. The theoretical curve (Hill and Liu, 2005) is a density of vibrational states $g(\omega)$, which differs significantly from the GDOS for hydrogen in the low energy part. The $g(\omega)$ at low energies originates mainly from the vibrations of heavy carbon atoms, and the eigenvectors for hydrogen in this energy range are smaller than for carbon. To find a best possible normalizing constant, the area under each peak, for both experimental and theoretical curve, was computed, and the normalizing constant was taken to be the ratio of areas under each peak. The proposed method is only an approximation to determining the normalization constant for collapsing different incident energy sets, and was not used for creation of final thermal scattering libraries. The resulting GDOS is therefore theory normalized, and can be seen in Fig. 4. It may be counterintuitive to use the
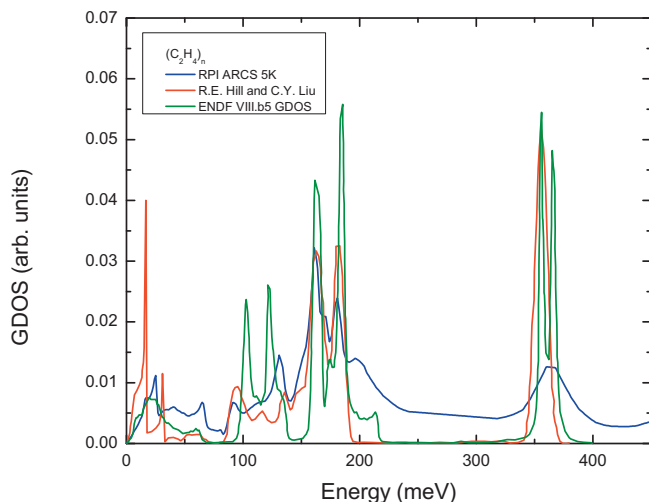

Fig. 4. Comparison of theoretical density of vibrational states, $g(\omega)$, versus experimentally derived GDOS at 5 K.

theoretical curve for the normalization of the experimentally obtained one, but this issue will be discussed more in the results section. The locations of the peaks are satisfying, where the differences in the height and the width of the peaks come from the facts that theoretical curve has no instrument resolution associated with it, and no multiple-phonon scattering effects are included. It is important to note that there are significant physical differences between RPI ARCS GDOS and ENDF/B-VIII.b5 gdos. Most significant differences are in the region from ≈ 80 to 140 meV, where the locations of the peaks in ENDF/B-VIII.b5 GDOS are significantly shifted when compared to Hill and Liu (2005) and RPI ARCS GDOS.

3.1.1. Library validation

In order to generate new thermal scattering libraries ($S(\alpha, \beta)$) for $(C_2H_4)_n$, NJOY2016 and MCNP6.1 were used. The main NJOY2016 modules used for $S(\alpha, \beta)$ generation were LEAPR, THERMR and ACER. LEAPR generated the $S(\alpha, \beta)$ data in ENDF format, THERMR calculated the pointwise thermal scattering data in PENDF format, while ACER generated the data in .ace format to be used with MCNP6.1. In order to verify the validity of newly created $S(\alpha, \beta)$ files, our group has constructed different MCNP models of the experimental setup, described in Wendorff et al. (2018).

The $(C_2H_4)_n$ experiment at ARCS resulted in a unique experimental GDOS derived from DDSCS measurements. The comparison between ENDF/B-VII.1, ENDF/B-VIII.5b, the NJOY processed library produced from our experiments, the NJOY processed library produced from theoretical curve from Hill and Liu (2005), and the experimental DDSCS is represented in Fig. 5.

The RPI $(C_2H_4)_n$ library improves upon the ENDF/B-VII.1 library, and agrees better with the DDSCS. This is expected because the evaluation was created from the same experimental data. Although RPI $(C_2H_4)_n$ does behave adequately, it's important to note that the GDOS from which the library was created already included multiple-phonon contributions (n > 1 events), which were also added by NJOY2016, resulting in double-counting the multiple-phonon contributions. This is the reason why the peaks at higher incident energies are smoothed out. When compared to ENDF/B-VIII.5b, RPI library performs as well or better than ENDF/B-VIII.5b library. For the incident energy of 250 meV and at the scattering angle 40.5 degrees in Fig. 5, in the region between ≈ 100 to 150 meV, the physical differences mentioned earlier between the RPI ARCS and ENDF/B-VIII.5b GDOS can be observed.

Furthermore, the total scattering cross section has been calculated using NJOY2016 and compared to the experimental total cross sections measured by Granada et al. (1987) and Herdade et al. (1973). Since the product of the NJOY2016 is the total scattering cross section, the following adjustment is needed in order to compare with the experimental total cross section, as seen in Ramić et al. (2016):

$$\sigma_{(C_2H_4)_n,t}(E) = 4 \times \left(\sigma_{H,s}^{NJOY2016}(E) + \sigma_{H,\gamma}^{ENDF}(E) \right) + 2 \times \left(\sigma_{C,t}^{ENDF}(E) \right).$$

(16)

As seen in Fig. 6, in the energy region below 10 meV, ENDF/B-VII.1 library deviates from the measurement. Both RPI $(C_2H_4)_n$ and ENDF/B-VIII.b5 library provide an improvement in this region, while agreeing reasonably with the experimental total cross section above the 10 meV region. What is important to notice is that the ENDF/B-VIII.b5 library reproduces total cross section correctly without having physically correct GDOS. All libraries do seem to fail to predict the structure in the experimental total cross section in the region between 100 and 300 meV, which is consistent with what Lavelle et al. (2013) reported. This is indicative of need to improve the NJOY2016 theoretical framework in order to reproduce the total cross section correctly. The theoretical GDOS evaluation does not perform as well as the other libraries do. The
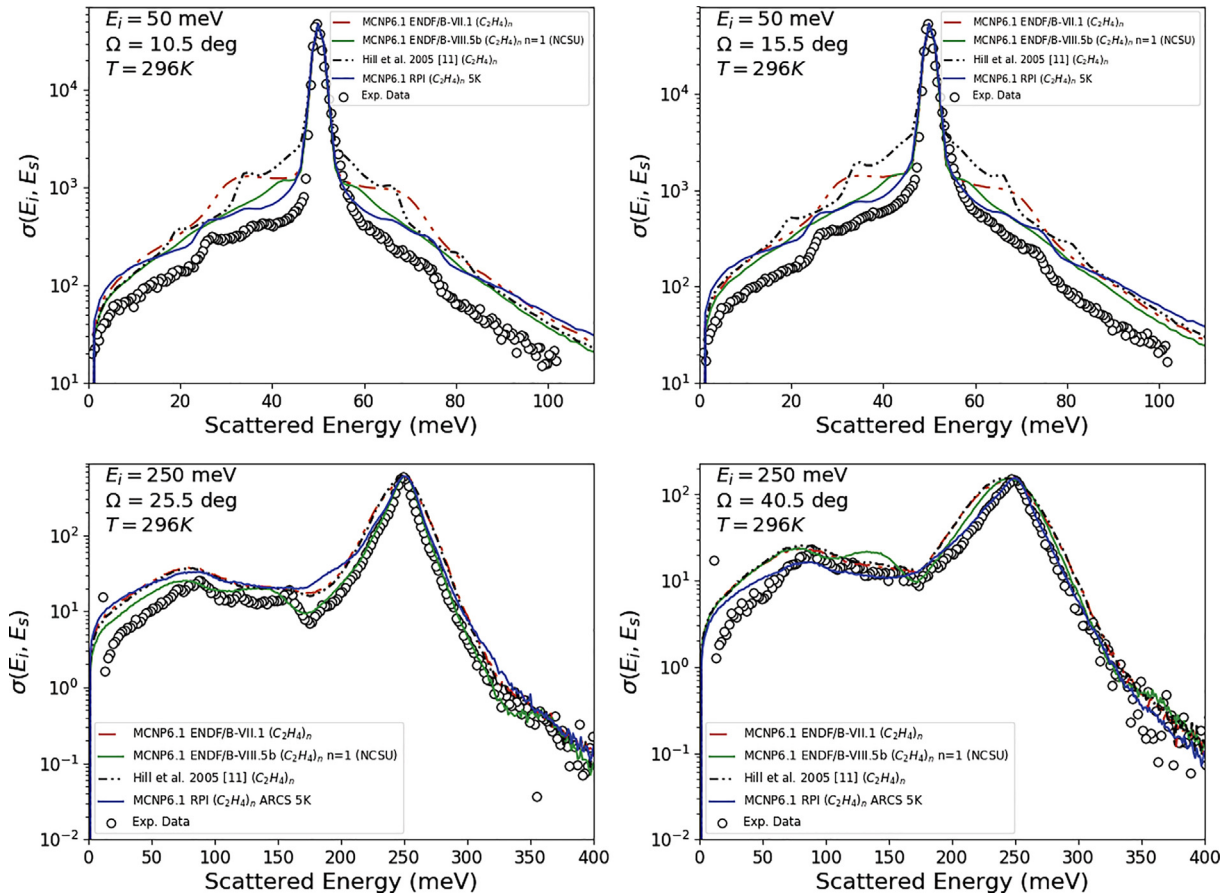
Fig. 5. DDSCS comparison at the 50 and 250 meV incident energies, at scattering angles 25.5 and 40.5 degrees.
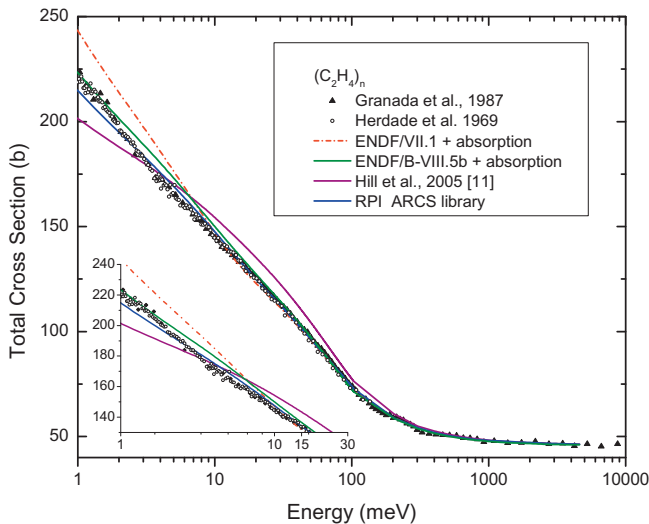

Fig. 6. Total scattering cross section of $(C_2H_4)_n$. RPI $(C_2H_4)_n$ library improves upon ENDF/B-VII.1 library in the lower energy region.

experimental GDOS, due to absence of a standardized normalization process, benefits from the normalization to the theoretical GDOS found in Hill and Liu (2005). Hill and Liu (2005) GDOS results in a sub-par library when compared to ENDF and the new RPI libraries.

Although it has been shown that RPI $(C_2H_4)_n$ library exhibits improvements in the double differential scattering cross section,

while also improving upon the total cross section of $(C_2H_4)_n$, additionally critical benchmarks have been conducted using all available $(C_2H_4)_n$ libraries. The results will be shown in Section 3.2.2.

3.2. VISION method

As can be seen in Section 3.1, the experimental data at ARCS and SEQUOIA have been measured using different incident energies, covering different regions of the (Q, ω) spectrum. Therefore, fragmentation makes the production of the uniform GDOS harder because there is no good established method to collapse all data sets onto the uniform (Q, ω) grid. Thus, there is a need to produce the experimental GDOS that doesn't suffer from those deficiencies. The VISION instrument at SNS has been designed to study vibrational dynamics of atoms in molecules of solids using neutrons, and is analogue to a infra-red or Raman spectrometer, Ramirez-Cuesta (2004). Because of the usage of the diffraction banks, the instrument can provide information on the positions of the atoms, and not only on dynamics. ARCS ans SEQUOIA have large Q coverage at elastic line and also give information on the neutron diffraction in addition to the INS data. Unlike ARCS and SEQUOIA, which have fixed incident energy, the incident energy at VISION is a white beam (neutron beam where the incident energy is a spectrum, not just one specific incident energy), while the final energy is set to a fixed low energy (32 cm^{-1} or 0.004 eV). The energy resolution of VISION instrument is constant at 1.5% $\Delta E/E$.

The experimentally measured quantity at the VISION instrument was transformed to $S(Q, \omega)$, and the obtained spectrum cov-
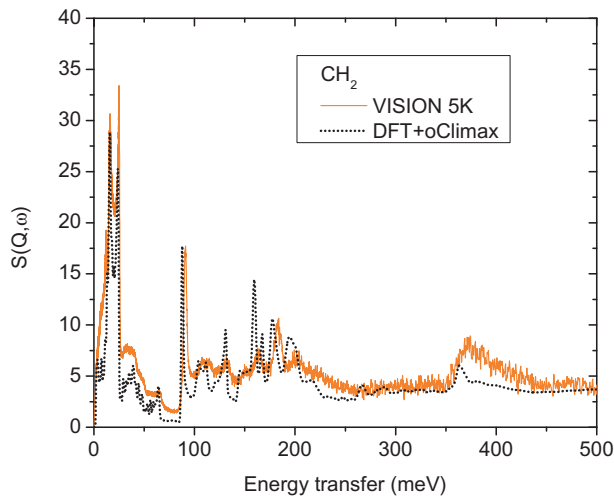
Fig. 7. Comparison of S(Q,ω) derived from measurements at VISION spectrometer and calculated using CASTEP and oClimax.

ers the whole energy range of interest. The example of the measured data for $(C_2H_4)_n$ can be seen in Fig. 7. The transformation from S(Q,ω) to the GDOS was done with Eqs. 14 and 15, and it is the same as in the case of ARCS and SEQUOIA. For all neutron spectrometers the change of energy and momentum transfer can be expressed as:

$$\hbar\omega = \frac{\hbar^2}{2m}(k_i^2 - k_f^2), \qquad \mathbf{Q} = \mathbf{k}_i - \mathbf{k}_f, \tag{17}$$

and for VISION, due to small final energy of scattered neutrons, the momentum transfer (in units 1/Å) can be related to energy transfer (in meV) as:

$$Q^2 \approx \frac{\omega}{2.07} \tag{18}$$

The comparison of GDOS obtained from VISION and ARCS can be seen in Fig. 8.

It is noticeable that relative positions of the peaks match quite well, although there are differences in the intensities of peaks. It should be noted that in Parker et al. (1996), it was shown that INS spectrum measured at TFXA (ISIS) of oriented $(C_2H_4)_n$ in the
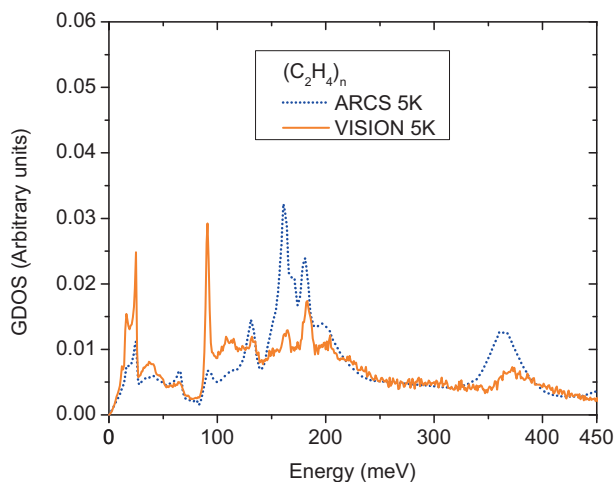

Fig. 8. The resulting $(C_2H_4)_n$ GDOS derived from measurements at VISION and ARCS instruments.

energy range 60–200 meV is dominated by the peak at 80 meV for the Q perpendicular to the c-axis of the sample, and for the Q——c-axis the features at 125–170 meV are larger. The difference in the derived GDOS between ARCS and VISION is due to different orientation of the quasi single-crystal (textured) sample relative to the neutron momentum transfer vector **Q**, which is almost perpendicular to the sample plane at VISION. At ARCS **Q** goes from being almost perpendicular (at the negative scattering angles) to being almost parallel (at the positive scattering angles) relative to the sample plane (which was 45 deg to the incident neutrons). Therefore, the sum over wide range of detectors at ARCS produces better 3D averaging of the data for the textured sample. The position of the C-H stretching peak in DFT calculation and in the INS spectrum at ARCS (and also SEQUOIA) are close to each other ≈360 meV, and at VISION the peak appears at slightly higher energy, ≈370 meV, and diminished intensity. The reason is that due to the large momentum transfer and large <u²> this peak is almost invisible in the VISION spectrum, and it is better seen in the ARCS spectrum at low **Q**.

Retrospectively, one can conclude that the collapsing method used for ARCS GDOS is not unreasonable. The VISION measurements can be possibly used to guide the collapsing method of data obtained at ARCS and SEQUOIA. An alternative method of using VISION data to collapse ARCS GDOS properly was tested, but the method did not produce significantly better results when compared to the results obtained using the normalization technique we described previously.

The true benefits of using the VISION instrument come from the ability to combine the VISION measurements and ab initio (Density Functional Theory, DFT) simulation in such manner that the VISION measurements can be used to validate and benchmark the underlaying DFT model and simulation. Unlike the infra-red or Raman spectroscopy, inelastic neutron scattering (INS) does not have any optical selection rules (all transitions should be observable); therefore, according to Ramirez-Cuesta (2004), INS represents a perfect test bed for DFT calculations of vibrational modes. The flowchart of the proposed method can be seen in Fig. 9.

According to Ramirez-Cuesta (2004), aClimax is used to interpret INS spectra taken at VISION- and TOSCA-like instruments. This is done by relying on DFT codes that produce atomic displacements and frequencies of atoms in the molecule during the simulation. The theory behind aCLimax was introduced in Ramirez-Cuesta (2004). Since June 2017 aClimax has been replaced by a newer version named oClimax, which has been used for the purposes of this report. As it can be observed in Fig. 7, there are small differences in the position of the peaks. The ab initio calculations carry some inherent errors that are mostly due to the potential functions used. According to Ramirez-Cuesta (2004), these errors can be reduced by "scaling" the calculated frequencies. By combining infra-red and Raman measurements, it is easier to associate the calculated transitions with the experimentally observed ones, in a manner producing a map of calculated frequencies over the INS spectrum. By recalculating the DFT spectra, changing the frequencies (positions of the peaks) to match the INS spectrum, and by keeping constant the values of DFT intensities (height of the peaks), the calculated spectrum is directly comparable to measured one at VISION. The emphasis is that this does not correspond to arbitrary manipulation of the spectra, but by the use of other spectroscopic techniques (infra-red and Raman), we fix the symmetry of the vibrational modes. It is important to note that the differences in peak positions do not come solely from DFT errors, but the differences could be a result of different structural properties of material measured versus DFT simulated material. The $(C_2H_4)_n$ material used for the experiments does not have perfect crystalline structure as does the structural setup used for DFT simulation.
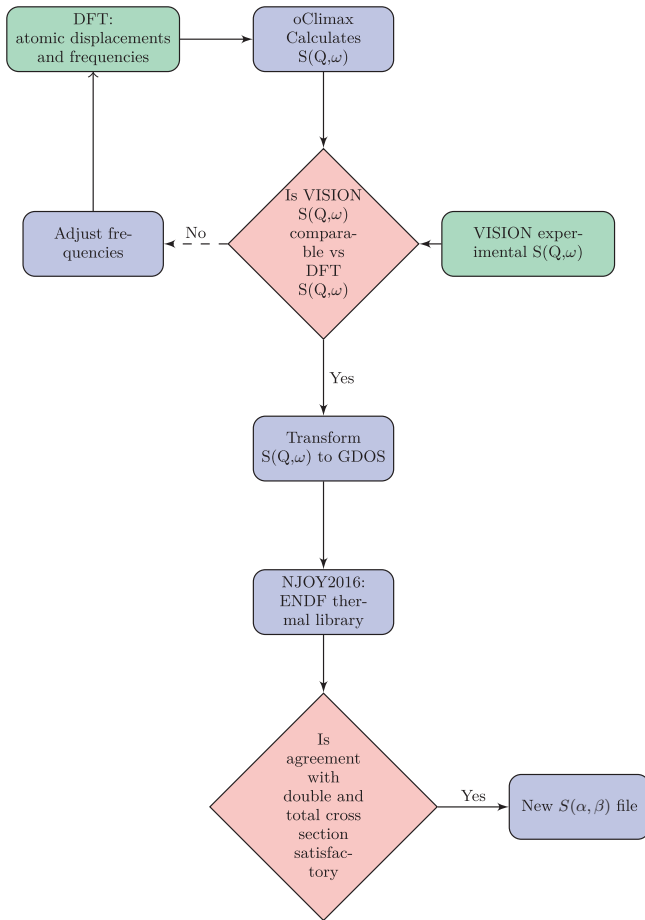
Fig. 9. The proposed method of utilizing VISION measurements and DFT calculations for production of new thermal scattering libraries.
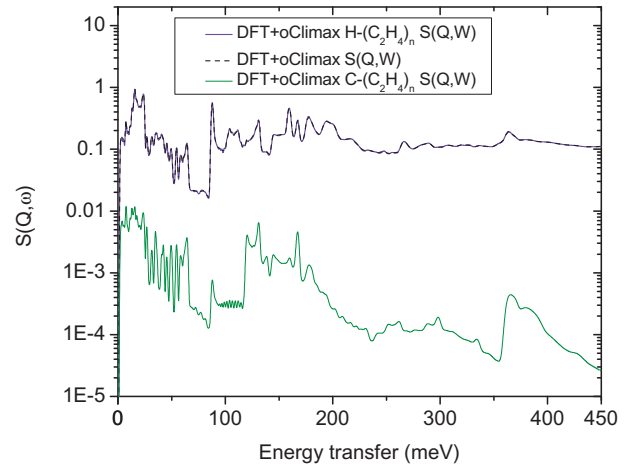

Fig. 10. Comparison of $(C_2H_4)_n$ $S(Q,\omega)$ vs. H-$(C_2H_4)_n$ $S(Q,\omega)$. The bottom curve shows partial contribution of carbon, (C-$(C_2H_4)_n$), to the total $(C_2H_4)_n$ $S(Q,\omega)$.

3.2.1. oClimax implementation

The $(C_2H_4)_n$ DFT simulations have been performed using CASTEP DFT code. CASTEP uses density functional perturbation theory (DFPT) to calculate phonons, which means that the simulation of the unit cell is sufficient, no need for computationally extensive supercells. The simulated unit cell consisted of 12 atoms making two polyethylene chains, and the exchange correlation (XC) energy functional used was PBE (Perdew, 1996). More details, as well as the input files, on the DFT calculations can be found in Ramić et al. (2018). The DFT simulation results were processed with oClimax, as suggested in the flowchart. The comparison between DFT + oClimax vs VISION $S(Q,\omega)$ can be seen in Fig. 7.

The important contributions that VISION method (DFT + oClimax) has are threefold: 1) the ability to determine partial contributions to GDOS, 2) the fact that oClimax, unlike aClimax, is able to calculate coherent scattering effects (not just determine $S(Q,\omega)$ in incoherent approximation, aClimax), which is a relatively new and unique contribution to the field, and 3) oClimax is able to calculate the multiple quantum events, or n > 1 modes.

Using oClimax, we can determine partial contributions of hydrogen and carbon to the total $(C_2H_4)_n$ $S(Q,\omega)$, which can be reduced to GDOS. The individual contributions vs total $S(Q,\omega)$ can be seen in Fig. 10.

From the Fig. 10 it can be seen that hydrogen is the main scatterer in $(C_2H_4)_n$, which is dominantly incoherent scatterer. The hydrogen contributions are higher due to the larger total scattering cross section of hydrogen, 82.02 barns, when compared to carbon total scattering cross section, 5.551 barns. Fig. 10 also shows us that carbon contributions are mostly constricted to lower energies.

$(C_2H_4)_n$ is dominantly incoherent scatterer due to hydrogens large incoherent scattering cross section of 80.27 barns. Using oClimax it is possible to determine incoherent versus coherent component of $S(Q,\omega)$, where the comparison can be seen in Fig. 11. As expected, for $(C_2H_4)_n$ coherent scattering effects are minimal and confined to the lower energies.

After the transformation from $S(Q,\omega)$ to GDOS, the resulting spectra can be seen in Fig. 12.

The Fig. 12 shows one of crucial advantages of DFT + oClimax method. From Fig. 12 it can be seen that we have successfully demonstrated that peak adjustment can be indeed performed, without breaking any symmetry of vibrational modes.

The other important observation is the effect of inclusion of multiple quantum events (n > 1 modes) on the shape of the spectrum. As it can be seen in the Fig. 13, n > 1 modes are responsible for smearing of sharp peaks, while also creating new peaks (i.e. peak at around 200 meV). The exact locations of the peaks and creation of new peaks is the reason why we still need experimental data. One could argue that doing just DFT + oClimax is sufficient, but with the experimental data we are able to validate our DFT calculation. If the results of DFT + oClimax method are not satisfactory, the experimental data can be used to improve the
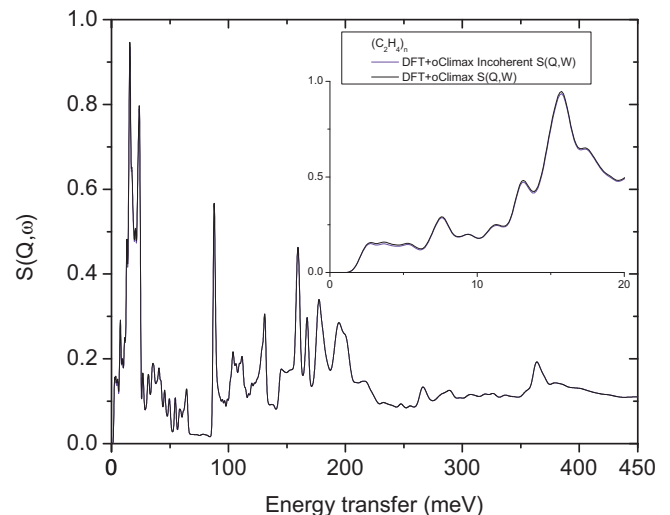
Fig. 11. Comparison of $(C_2H_4)_n$ $S(Q,\omega)$ with included coherent scattering component vs. calculation done with coherent scattering component excluded.
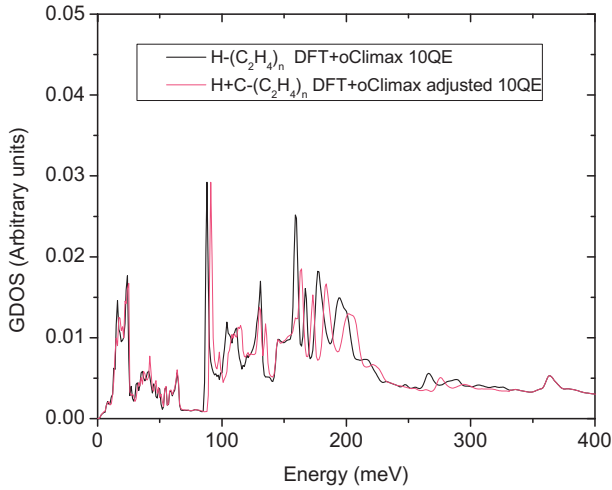
Fig. 12. Comparison of GDOS calculated using CASTEP and oClimax, where the effects of peak adjusting can be seen.
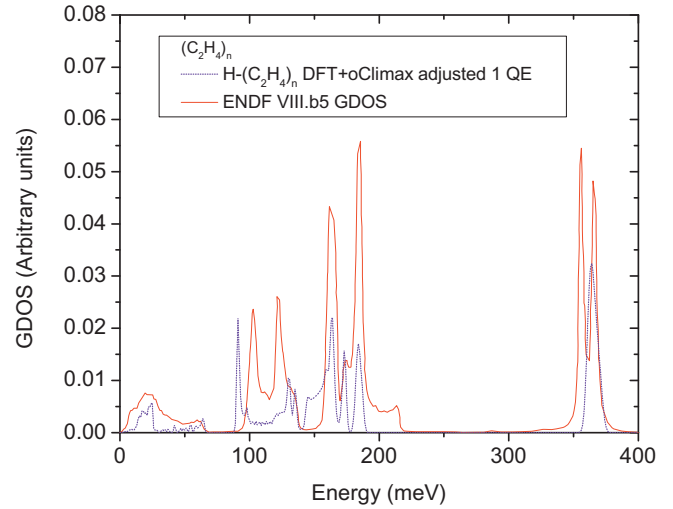

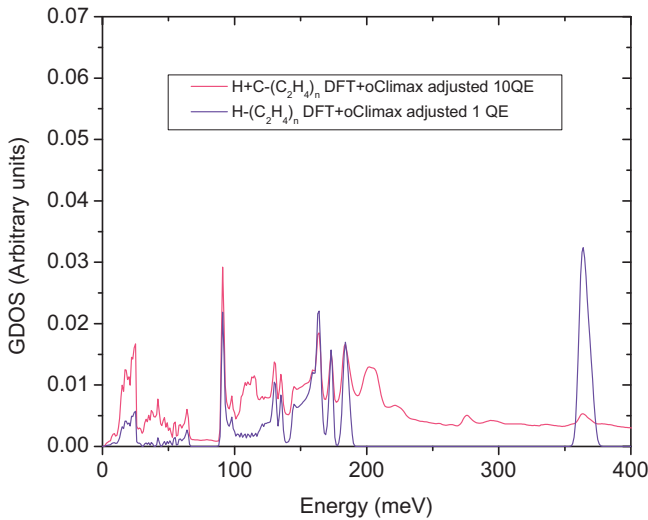**Fig. 14.** Comparison of ENDF/B-VIII.b5 GDOS and DFT + oClimax GDOS.

Fig. 13. Comparison of GDOS calculated using CASTEP and oClimax, where the effects of an expansion up to 10 quantum events (n = 10) can be seen.

DFT + oClimax calculation. For the remainder of paper, this adjusted GDOS (and quantities related to the library created from the adjusted GDOS) will be Referenced to as *RPI (H + C)-(C₂H₄)ₙ DFT + oClimax*, or a *DFT + oClimax* method (GDOS, library, etc.). The ENDF/B-VIII.b5 GDOS is based only on one quantum event (n = 1), and the comparison between ENDF/B-VIII.b5 GDOS and DFT + oCLimax n = 1 GDOS can be seen in Fig. 14. As previously noted, Fig. 14 reaffirms physical irregularities of ENDF/B-VIII.b5 GDOS, where the region between ≈80 and 140 meV is miscalculated, while extra area is added in the region above 180 meV.

3.2.2. Library validation

To validate the DFT + oClimax GDOS we run the GDOS through NJOY2016 to create new thermal scattering library, that is further validated using MCNP. The DDSCS for different libraries was simulated using MCNP and comparison can be seen in Fig. 15. Generally, DFT + oCLimax 1QE (n = 1) is the best performing library. The ENDF/B-VIII.b5 library fails to reproduce some of the structural information (location of certain peaks), while DFT + oCLimax 1QE library shows all the significant structural information (especially at higher incident energy, 250 meV), although some of the peaks are exaggerated at lower incident energies.

The most important test of the new thermal scattering libraries is to see how well the calculated total cross sections match the experimental data. Since we are capable of producing thermal libraries for each moderating material from its respective partial GDOS, Eq. 16 has to be adjusted accordingly:

$$\sigma_{(C_2H_4)_n,t}(E) = 4 \times \left(\sigma_{H,s}^{NJOY2016}(E) + \sigma_{H,\gamma}^{ENDF}(E) \right) + 2$$
$$\times \left(\sigma_{C,s}^{NJOY2016}(E) + \sigma_{C,\gamma}^{ENDF}(E) \right). \tag{19}$$

The RPI DFT (H + C)-(C₂H₄)ₙ library was created from separate H-(C₂H₄)ₙ and C-(C₂H₄)ₙ phonon spectrums, derived with the help of oClimax. From Fig. 16 it is noticeable that the RPI DFT (H + C)-(C₂H₄)ₙ library performs significantly better then ENDF VII.1 library across the whole energy region. The most improvement is seen in the region below 10 meV where the RPI DFT (H + C)-(C₂H₄)ₙ and newest ENDF library perform significantly better. Many of the neutrons inside a reactor have energy spread of approximately 50 meV, and both RPI libraries perform well in that region. The extent of improvements to the total cross section calculation, that originate from improved DFT calculations, is limited by the NJOY2016 post-processing of DFT + oCLimax GDOS. NJOY2016, in order to produce new thermal libraries to be used with MCNP, uses the incoherent approximation to calculate S(Q,ω) from DFT + oClimax GDOS. In order to obtain better total and double differential cross sections, it is suggested to improve NJOY2016 by relaxing the incoherent approximation and improving theoretical implementation of phonon expansion, which at the moment may not be implemented perfectly (arguably incorrect ENDF/VIII.0 library GDOS reproduces the total cross section correctly, while none of the libraries reproduce the structure in the region from 100 to 300 meV correctly, which can be observed in Figs. 6 and 16). What is important to notice is that the ENDF/B-VIII.b5 library reproduces total cross section correctly without having physically correct GDOS. As we can see from Fig. 14, the locations and shapes of the peaks are off from the experimentally derived GDOS.

The final test of the libraries created would be to perform critical benchmarks on them. The work is described in more detail in Wendorff et al. (2018). The measured quantity was K_{eff}; the critical benchmarks that contain (C₂H₄)ₙ were chosen using the Database for the International Handbook of Evaluated Criticality Safety Benchmark Experiments (DICE) (DICE, 1996).

Fig. 17 shows that simulations without a scattering kernel (free gas model) resulted in overestimating the K_{eff}, while the RPI ARCS
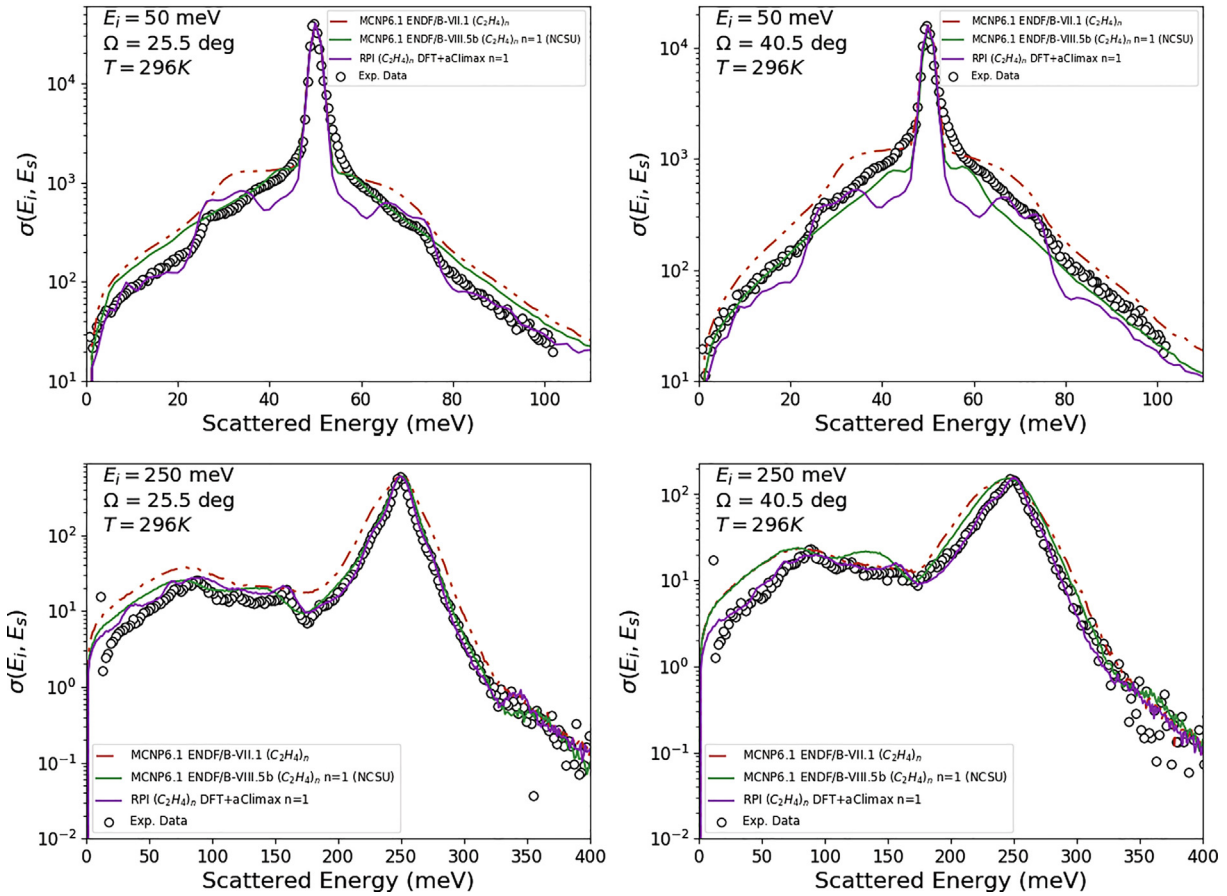
Fig. 15. DDSCS comparison at the 50 and 250 meV incident energies, at scattering angles 25.5 and 40.5 degrees.
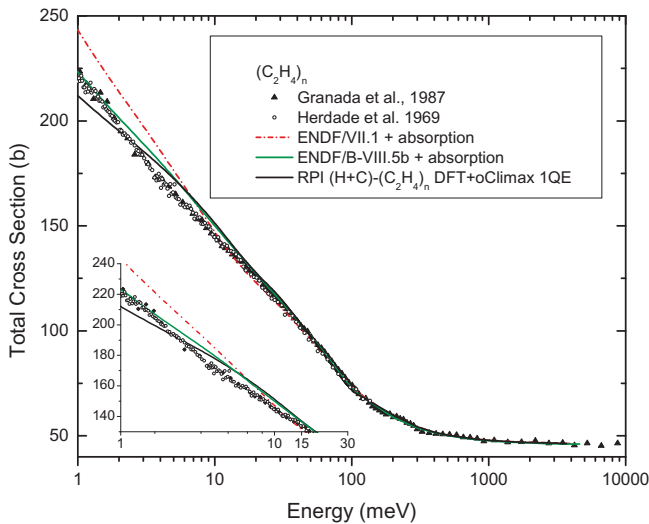

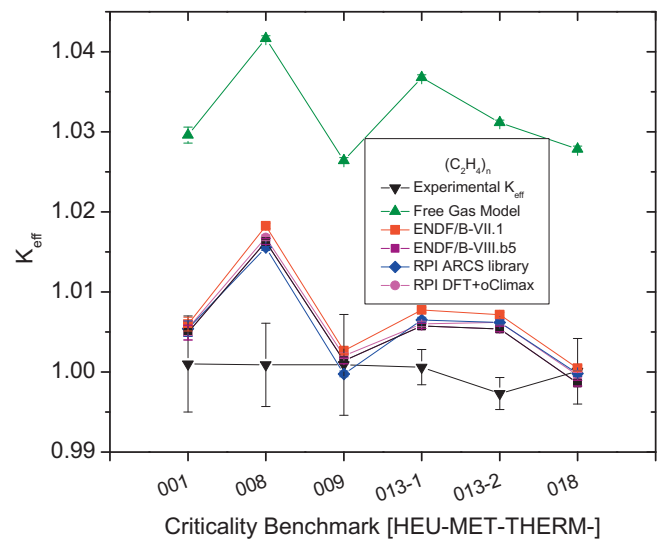**Fig. 16.** Total scattering cross section of $(C_2H_4)_n$.

Fig. 17. K_{eff} comparison for $(C_2H_4)_n$ critical benchmarks. Each x-axis point represents a different $(C_2H_4)_n$ moderated critical benchmark. The uncertainty is only from the experimental benchmark.

library, RPI DFT + oClimax, and the ENDF/B-VIII.b5 library consistently performed slightly better than the ENDF/B-VII.1 library. The summary of K_{eff} values can be seen in Table 2. Although these libraries perform better, this is probably due to the fact that the total cross section changed, systematically lowering down the calculated K_{eff} values. This is also reflected in the fact that they all have similar K_{eff} values.

The DFT + oClimax method has shown its great potential, and we believe it is an essential tool to be used in generation of new thermal scattering libraries. An advantage of great importance for this method is to create the partial GDOS for constituent particles; for example, H in $(C_2H_4)_n$ or C in $(C_2H_4)_n$, while using experimental data to guide and validate the DFT + oClimax method.

Table 2
K_{eff} comparison for $(C_2H_4)_n$ critical benchmarks.

Critical benchmark	$(C_2H_4)_n$ library	K_{eff}	Std. dev.
H-M-T-001	Experimental	1.001	0.006
H-M-T-001	ENDF/B-VII.1	1.00598	8.7E−4
H-M-T-001	ENDF/B-VIII.b5	1.00493	9.2E−4
H-M-T-001	RPI DFT + oClimax	1.00549	9.2E−4
H-M-T-001	RPI ARCS library	1.00541	9.7E−4
H-M-T-001	Free Gas Model	1.02959	9.9E−4
H-M-T-008	Experimental	1.0009	0.0052
H-M-T-008	ENDF/B-VII.1	1.01825	3.5E−4
H-M-T-008	ENDF/B-VIII.b5	1.01629	3.6E−4
H-M-T-008	RPI DFT + oClimax	1.01677	3.5E−4
H-M-T-008	RPI ARCS library	1.01555	3.5E−4
H-M-T-008	Free Gas Model	1.04166	3.5E−4
H-M-T-009	Experimental	1.0009	0.0063
H-M-T-009	ENDF/B-VII.1	1.00265	3.6E−4
H-M-T-009	ENDF/B-VIII.b5	1.0014	3.6E−4
H-M-T-009	RPI DFT + oClimax	1.00204	3.4E−4
H-M-T-009	RPI ARCS library	0.99976	3.5E−4
H-M-T-009	Free Gas Model	1.02642	3.5E−4
H-M-T-013-1	Experimental	1.0006	0.0022
H-M-T-013-1	ENDF/B-VII.1	1.00774	3.4E−4
H-M-T-013-1	ENDF/B-VIII.b5	1.00576	3.3E−4
H-M-T-013-1	RPI DFT + oClimax	1.006	3.3E−4
H-M-T-013-1	RPI ARCS library	1.00651	3.2E−4
H-M-T-013-1	Free Gas Model	1.03679	3.2E−4
H-M-T-013-2	Experimental	0.9973	0.002
H-M-T-013-2	ENDF/B-VII.1	1.00715	3.3E−4
H-M-T-013-2	ENDF/B-VIII.b5	1.00538	3.4E−4
H-M-T-013-2	RPI DFT + oClimax	1.00621	3.5E−4
H-M-T-013-2	RPI ARCS library	1.0062	3.4E−4
H-M-T-013-2	Free Gas Model	1.03116	3.2E−4
H-M-T-018	Experimental	1.0001	0.0041
H-M-T-018	ENDF/B-VII.1	1.00048	3.5E−4
H-M-T-018	ENDF/B-VIII.b5	0.99861	3.5E−4
H-M-T-018	RPI DFT + oClimax	0.9996	3.5E−4
H-M-T-018	RPI ARCS library	0.9998	3.5E−4
H-M-T-018	Free Gas Model	1.02785	3.6E−4

4. Conclusion and future work

The ARCS, SEQUOIA, and VISION experiments at SNS provide a comprehensive insight into the thermal neutron scattering properties of $(C_2H_4)_n$. The resulting thorough analysis of the experimental data has led to an improved $(C_2H_4)_n$ library with improved double differential and total cross sections. While the benchmarks show an improvement in K_{eff} calculation, definite statements about impact on criticality cannot be made, because the available benchmarks might not be sensitive enough to $(C_2H_4)_n$.

This work on $(C_2H_4)_n$ lays the foundation for accurately predicting the thermal scattering law of different moderator materials based on integration of scattering experiments and DFT theory. Two different methods of generating new thermal libraries for $(C_2H_4)_n$ have been successfully demonstrated, including their deficiencies. These procedures are developed in such a way that they can be applied to different moderator materials. The DFT + oClimax method has been shown to be the most complete method, with the least deficiencies, when compared to a purely experimental or simulation approach that represents a "bridge" between experiments and simulations. The importance of the DFT + oClimax method is in the fact that it can be validated against all data measured at VISION, ARCS and SEQUOIA, and experimental total scattering cross section measurements. An additional, not yet utilized, benefit of the method is in the fact that DFT + oClimax calculated $S(Q, \omega)$ can be converted directly to $S(\alpha, \beta)$, and hence used directly with NJOY2016. The DFT + oClimax method is a synergistic and comprehensive method that employs simulations and experimental data to create thermal scattering laws for existing and new moderator materials.

References

Abernathy, D.L., Stone, M.B., Loguillo, M.J., Lucas, M.S., Delaire, O., Tang, X., Lin, J.Y.Y., Fultz, B., 2012. Design and operation of the Wide Angular-Range Chopper Spectrometer (ARCS) at the Spallation Neutron Source. Rev. Sci. Instrum. 83. https://doi.org/10.1063/1.3680104.

Azuah, R.T., Kneller, L., Dimeo, R., 2009. Dave: a comprehensive software suite for the reduction, visualization, and analysis of low energy neutron spectroscopic data. J. Res. Nat. Inst. Stand. Technol. 114, 341–358.

Chadwick, M., Herman, M., Obložinský, P., Dunn, M., Danon, Y., Kahler, A., Smith, D., Pritychenko, B., Arbanas, G., Arcilla, R., Brewer, R., Brown, D., Capote, R., Carlson, A., Cho, Y., Derrien, H., Guber, K., Hale, G., Hoblit, S., Holloway, S., Johnson, T., Kawano, T., Kiedrowski, B., Kim, H., Kunieda, S., Larson, N., Leal, L., Lestone, J., Little, R., McCutchan, E., MacFarlane, R., MacInnes, M., Mattoon, C., McKnight, R., Mughabghab, S., Nobre, G., Palmiotti, G., Palumbo, A., Pigni, M., Pronyaev, V., Sayer, R., Sonzogni, A., Summers, N., Talou, P., Thompson, I., Trkov, A., Vogt, R., van der Marck, S., Wallner, A., White, M., Wiarda, D., Young, P., 2996. ENDF/B-VII.1 nuclear data for science and technology: Cross sections, covariances, fission product yields and decay data. Nucl. Data Sheets 112, 2887–2996. https://doi.org/10.1016/j.nds.2011.11.002.

Database for the International Criticality Safety Benchmark Evaluation Project (DICE), howpublished= http://icsbep.inel.gov/ (accessed: 2017-05-03).

Goorley, T., James, M., Booth, T., Brown, F., Bull, J., Cox, L.J., Durkee, J., Elson, J., Fensin, M., Forster, R.A., Hendricks, J., Hughes, H.G., Johns, R., Kiedrowski, B., Martz, R., Mashnik, S., Mckinney, G., Pelowitz, D., Prael, R., Sweezy, J., Waters, L., Wilcox, T., Zukaitis, T., 2016. Features of mcnp6. Ann. Nucl. Energy 87, 772–783. https://doi.org/10.1016/j.anucene.2015.02.020.

Granada, J., Dawidowski, J., Mayer, R., Gillette, V., 1987. Thermal neutron cross section and transport properties of polyethylene. Nucl. Instrum. Methods Phys. Res., Sect. A 261, 573–578.

Granroth, G., Kolesnikov, A., Sherline, T., Clancy, J., Ross, K., Ruff, J., Gaulin, B., Nagler, S., 0120. Sequoia: a newly operating chopper spectrometer at the SNS. J. Phys: Conf. Ser. 251, 012058. URL http://stacks.iop.org/1742-6596/251/i=1/a=012058.

Herdade, S., Vinhas, L., Rodrigues, C., Amaral, L., 1973. Neutron cross sections of polyethylene and light water in the energy range $8.2 \times 10^{\wedge}(-4)$ to 0.13 Ev. IEA.

Hill, R.E., Liu, C.-Y., 2005. Temperature-dependent neutron scattering cross-sections for polyethylene. Nucl. Instrum. Methods Phys. Res., Sect. A 538, 686–691. https://doi.org/10.1016/j.nima.2004.08.125.

Kirouac, G.J., Moore, W.E., Seemann, K.W., 1966. Inelastic scattering cross sections for polyethylene and water in the gas transition region. Nucl. Sci. Eng. (U.S.) 25.

Lavelle, C., Liu, C.-Y., Stone, M., 2013. Toward a new polyethylene scattering law determined using inelastic neutron scattering. Nucl. Instrum. Methods Phys. Res., Sect. A 711, 166–179. https://doi.org/10.1016/j.nima.2013.01.048.

MacFarlaneandA, R., Kahler, A., 2010. Methods for processing ENDF/B-VII with NJOY. Nucl. Data Sheets 111, 2739–2890. https://doi.org/10.1016/j.nds.2010.11.001.

Parker, S.F., 1996. Inelastic neutron scattering spectra of polyethylene. J. Chem. Soc., Faraday Trans. 92, 1941–1946. https://doi.org/10.1039/FT9969201941.

Perdew, J.P., Burke, K., Ernzerhof, M., 1996. Generalized gradient approximation made simple. Phys. Rev. Lett. 77, 3865–3868. https://doi.org/10.1103/PhysRevLett.77.3865.

Ramić, K., 2018. From Experiments to DFT Simulations: Comprehensive Overview of Thermall Scattering For Neutron Moderator Materials. Rensselaer Polytechnic Institute (Ph.D. dissertation).

Ramić, K., Wendorff, C., Danon, Y., Liu, L., 2016. Improvements to thermal neutron scattering law of CH^2. Trans. Am. Nucl. Soc. 115, 687–688.

Ramirez-Cuesta, A., 2004. aClimax 4.0.1, the new version of the software for analyzing and interpreting INS spectra. Comput. Phys. Commun. 157, 226–238. https://doi.org/10.1016/S0010-4655(03)00520-4.

Seeger, P.A., Daemen, L.L., Larese, J.Z., 2009. Resolution of VISION, a crystal-analyzer spectrometer. Nucl. Instrum. Methods Phys. Res., Sect. A 604, 719–728. https://doi.org/10.1016/j.nima.2009.03.204.

Squires, G.L., 2012. Introduction to the Theory of Thermal Neutron Scattering. Cambridge University Press. https://doi.org/10.1017/CBO9781139107808.

Wendorff, C., Ramić, K., Liu, L., Danon, Y., Kolesnikov, A.I., Abernathy, D., 2018. Improved experimental data for accurate thermal scattering kernel evaluations of water, polyethylene, and quartz.